Check for updates

NANO · MICRO small
www.small-journal.com

Microfluidic Generation of Monodisperse Nanobubbles by Selective Gas Dissolution

*Jiang Xu, Alinaghi Salari, Yanjie Wang, Xiaolin He, Liam Kerr, Ali Darbandi, Al C. de Leon, Agata A. Exner, Michael C. Kolios, Darren Yuen, and Scott S. H. Tsai**

Nanotechnology currently enables the fabrication of uniform solid nanoparticles and liquid nano-emulsions, but not uniform gaseous nanobubbles (NBs). In this article, for the first time, a method based on microfluidics that directly produces monodisperse NBs is reported. Specifically, a two-component gas mixture of water-soluble nitrogen and water-insoluble octafluoropropane as the gas phase are used in a microfluidic bubble generator. First, monodisperse microbubbles (MBs) with a classical microfluidic flow-focusing junction is generated, then the MBs shrink down to ≈100 nm diameter, due to the dissolution of the water-soluble components in the gas mixture. The degree of shrinkage is controlled by tuning the ratio of water-soluble to water-insoluble gas components. This technique maintains the monodispersity of the NBs, and enables precise control of the final NB size. It is found that the monodisperse NBs show better homogeneity than polydisperse NBs in in vitro ultrasound imaging experiments. Proof-of-concept in vivo kidney imaging is performed in live mice, demonstrating enhanced contrast using the monodisperse NBs. The NB monodispersity and imaging results make microfluidically generated NBs promising candidates as ultrasound contrast and molecular imaging agents.

1. Introduction

Nanobubbles (NBs) are generally considered to be bubbles with diameters less than 10^3 nm. Due to the unique features of NBs, such as high internal pressure, large surface-to-volume ratio, and high chemical and bio-activity,[1] NBs find utility in many important fields such as surface physics[2] and chemistry,[3,4] water treatment,[5] surface cleaning,[6] food processing,[7] and nanomedicine.[8] Among these applications, one significant utility of NBs is in clinical diagnostics,[9] where NBs are introduced into blood vessels as ultrasound contrast agents (UCAs),[10] for contrast-enhanced ultrasound (CEUS) imaging.[11] Due to their ability to extravasate out of the bloodstream, NBs may also be well-suited for ultrasound molecular imaging.[12]

Specifically, NBs show greater promise than microbubbles (MBs) in molecular imaging of diseases, such as cancer imaging.[13] MBs are intravascular contrast agents because of their larger size, while NB can in principle penetrate through blood vessels to target cells directly, owing to their smaller size and ability to extravasate in tissues due to the enhanced permeability retention (EPR) effect.[14–16]

The ability to produce monodisperse NBs for drug delivery may achieve significantly improved dose precision.[17] Therapeutic agents can be loaded on, or conjugated to, the surfaces of NBs, and released via ultrasound-induced cavitation. The size

Dr. J. Xu,[+] Dr. A. Salari, Y. Wang, L. Kerr, Prof. M. C. Kolios, Prof. S. S. H. Tsai
Institute for Biomedical Engineering
Science and Technology (iBEST)—a partnership between Ryerson University and St. Michael's Hospital
Toronto, Ontario M5B 1W8, Canada
E-mail: scott.tsai@ryerson.ca

Dr. J. Xu, L. Kerr, Prof. S. S. H. Tsai
Department of Mechanical and Industrial Engineering
Ryerson University
Toronto, Ontario M5B 2K3, Canada

Dr. J. Xu, Dr. A. Salari, Y. Wang, X. He, L. Kerr, Prof. M. C. Kolios, Prof. D. Yuen, Prof. S. S. H. Tsai
Keenan Research Centre for Biomedical Science
Unity Health Toronto
Toronto, Ontario M5B 1W8, Canada

The ORCID identification number(s) for the author(s) of this article can be found under https://doi.org/10.1002/smll.202100345.

[+]Present address: Department of Systems Biology, Harvard Medical School, Boston, MA 02115, USA

DOI: 10.1002/smll.202100345

Dr. A. Salari
Biomedical Engineering Graduate Program
Ryerson University
Toronto, Ontario M5B 2K2, Canada

Y. Wang, Prof. M. C. Kolios
Department of Physics
Ryerson University
Toronto, Ontario M5B 2K3, Canada

X. He, Prof. D. Yuen
Division of Nephrology
Department of Medicine
Unity Health Toronto and University of Toronto
Toronto, Ontario M5B 1W8, Canada

Dr. A. Darbandi
Nanoimaging Centre
The Hospital for Sick Children
Peter Gilgan Centre for Research & Learning
Toronto, Ontario M5G 0A4, Canada

Dr. A. C. de Leon, Prof. A. A. Exner
Department of Radiology
Case Western Reserve University
Cleveland, Ohio 44106, USA

 © 2021 Wiley-VCH GmbH

of bubbles in a monodisperse population of drug-conjugated NBs may be tuned to maximize the NB response to the ultrasound exposure parameters, such as pressure and excitation frequency, to optimize the efficiency of drug delivery.

It has been shown that monodisperse MBs have a more uniform acoustic response and increased imaging sensitivity compared to polydisperse MBs.[18,19] Therefore, it is expected that a similar effect would also apply to monodisperse NBs when compared to polydisperse NBs. However, despite the potential applications of monodisperse NBs in medicine, to date, there are no reports of the generation of monodisperse NBs that can simultaneously meet the requirements of simplicity, monodispersity, and high throughput (i.e., $\approx 10^3$ s^{-1}).[10] Current methods for producing NBs have various limitations.

High-frequency mechanical agitation at the gas/water interface of a surfactant solution is the most commonly used method to produce bulk NB solutions for ultrasound imaging applications.[20] While simple and effective, this protocol produces a polydisperse mixture of MBs and NBs.[21] The use of these heterogeneous bubbles requires further centrifugation[22] for isolation of bubbles of the desired size range.

Solvent exchange technique,[23–25] which is used to generate surface NBs, relies on the difference in gas solubility in water versus in organic solvents to precipitate gas out of the solution and form NBs. This technique produces a trace number of polydisperse NBs, and lacks the ability to sustain production. Thus, this approach is limited to the generation of NBs for static and qualitative surface characterization studies.

A similar problem exists in the method of degassing and temperature change,[26] which relies on the differences in gas solubility corresponding to pressure or temperature changes. The electrochemical method[27,28] achieves stable generation of NBs; however, the method relies on the reduction of protons or oxidation of precursor molecules, which limits its universality and production throughput.

Plasmonic NBs generated in tissues in situ, is a recent development of nanosurgery and detection.[17,29,30] This method requires the delivery of nanoparticle clusters and follow-up laser perturbation to generate NBs, which only have a lifetime of around several milliseconds, rendering it a complex and inefficient protocol. In summary, while many approaches are proposed and utilized to make NBs, creating monodisperse NBs with tunable sizes continues to be challenging.

Microfluidics (MF) is utilized as a tool to generate monodisperse MBs at high throughput, and customize MB size,[31] especially for ultrasound imaging applications.[32,33] Generally, the size of a bubble generated in a microfluidic flow-focusing geometry is proportional to the size of orifice, gas flow rate, and gas–liquid interfacial tension, and the bubble size is inversely related to the liquid flow rate and viscosity.[10,34]

However, due to the resolution limitations[35] and material properties used in soft lithography,[36] simply "scaling down" or "splitting"[37] from MBs to NBs is not trivial. To date, the minimum size of bubbles produced by microfluidics is still far above the nanoscale, at around a few microns.[38–40] Efforts have been made to produce NBs indirectly by first generating nanodroplets through a microfluidic nozzle, and then vaporizing the nanodroplets.[41] Although this approach results in a relatively high bubble concentration (i.e., $\approx 10^8$ mL^{-1}), this method does not enable control of the size distribution at the nanoscale. Furthermore, the mechanism of thermally-induced phase change limits usage to gases with boiling points close to room temperature, which prevents application of the approach as a universal method.

Here, we describe a microfluidic approach to first generate monodisperse MBs, then shrink the MBs into monodisperse NBs. Our technique draws inspiration from earlier work[42–46] showing that dispersions (i.e., emulsions and bubbles) that contain highly-soluble components in the discontinuous phase, can shrink significantly as the highly-soluble component leaves the dispersions and dissolves in the continuous phase. Following this concept, we design a gas mixture of two components: a high aqueous phase solubility gas, and a low aqueous phase solubility gas. With precise regulation of the ratio of high and low solubility gases, and optimized control of flow rates, gas pressure, and gas solubility, we achieve tunable NB sizes.

Notably, we achieve an MBs-to-NBs volume shrinkage ratio of up to 10^7, and obtain both monodispersity and relatively high throughput. In in vitro phantom models, the monodisperse NBs exhibit comparable stability, and improved contrast homogeneity, compared to polydisperse NBs. Finally, in in vivo proof-of-concept tests of the monodisperse NBs in mice, the NBs demonstrate good utility as UCAs.

2. Experimental Section

2.1. Fabrication of Microfluidic Devices

The microfluidic geometry was designed using AutoCAD (AutoCAD 2010, Autodesk, Inc., Dan Rafael, CA, USA) and printed onto a transparent photomask (25400 dpi, CAD/ART Services Inc., Bandon, OR, USA). Then a 50 μm thick film of SU-8 2050 (MicroChem, MA, USA) was spin-coated on a silicon wafer, which was then patterned by UV light through the photomask using conventional soft lithography techniques. A 5 mm thick layer of PDMS (polydimethylsiloxane, Sylgard 184 silicone elastomer kit, Dow Corning, Midland, MI, USA) was poured onto the patterned wafer, which was then baked in an oven at 70 °C for 2 h. After curing, the pattern on the wafer was transferred to the PDMS slab.

A gas inlet, lipid solution inlet, and an outlet were punched on the PDMS slab using a 1-mm diameter biopsy punch (Integra Miltex, Inc., Rietheim-Weilheim, Germany). After oxygen plasma (Harrick Plasma, Ithaca, NY, USA) treatment for 60 s, the PDMS slab was bonded to a glass microscope slide to complete the microfluidic chip (**Figure 1**a–b).

2.2. Preparation of Lipid Solutions

The basis of the lipid formulation was a solution that was originally optimized for the high-frequency mechanical agitation NB formation method, described in the existing literature.[11,47] This formation was modified to satisfy the interfacial tension and viscosity requirements for microfluidic bubble generation.

The modified lipid mixture was prepared in a glass vial by mixing 60.1 mg of 1,2-dipalmitoyl-sn-glycero-3-phosphocholine (DPPC), 10 mg of 1,2-dipalmitoyl-sn-glycero-3-phosphate

© 2021 Wiley-VCH GmbH

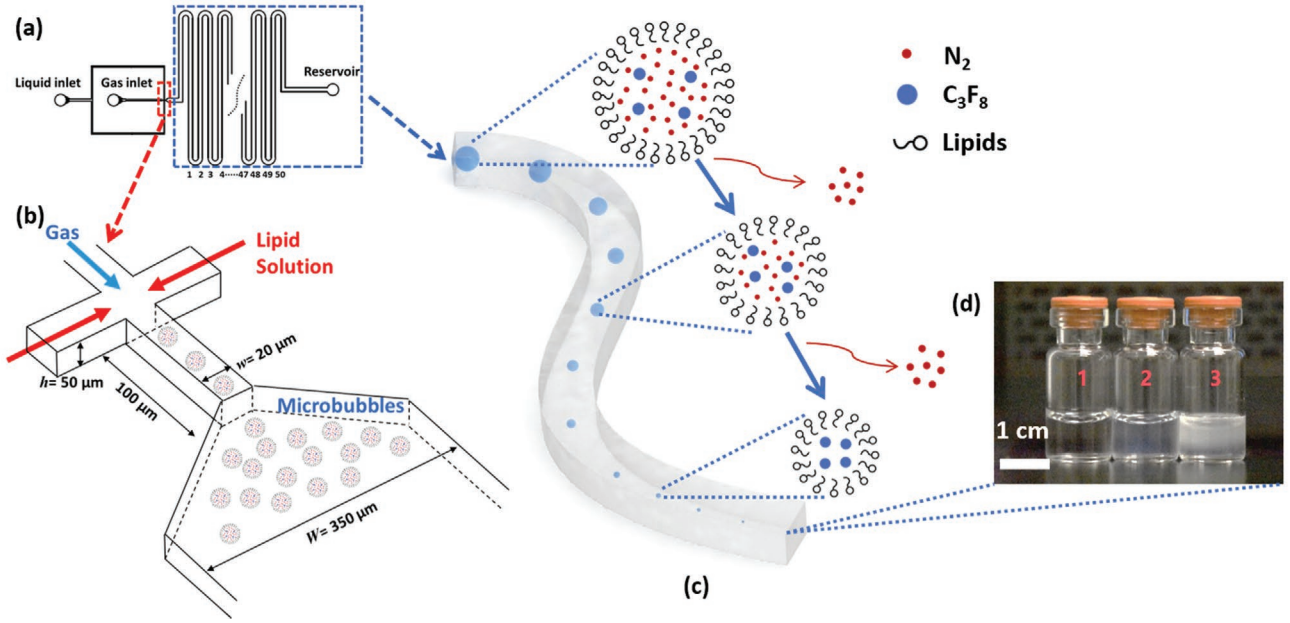

Figure 1. Schematic diagram of the microfluidic NB generator. a) An MB generation platform with a serpentine shrinkage channel. There are 50 turns in the serpentine channel, and the total serpentine channel length $L = 620$ mm; b) Dimensions of the MB generation orifice: orifice width $w = 20$ µm, channel height $h = 50$ µm, and serpentine channel width $W = 350$ µm; (c) Illustration showing MBs shrinking down to NBs (see Video S1, Supporting Information). Dissolution of N_2 from the mixed gas-core MBs leads to the shrinkage of the MBs down to the nanoscale. Insoluble C_3F_8 constitutes the final equilibrium gas core of NBs. d) Examples of NB solutions collected from the outlet. Glass vials numbered 1, 2, and 3 represent a blank lipid solution (as a control group), NB solution containing ≈100 nm diameter NBs, and NB solution containing ≈200 nm diameter NBs, respectively.

(DPPA), 20 mg of 1,2-dipalmitoyl-sn-glycero-3-phosphoethanolamine (DPPE), and 10 mg of 1,2-distearoyl-sn-glycero-3-phosphoethanolamine-*N*-[carboxy(polyethylene glycol)-2000] (DSPE-mPEG-2000). DPPE was purchased from Corden-Pharma, Switzerland, and other lipids were purchased from Avanti Polar Lipids, Inc., Alabama, USA. 15 mL of Dichloromethane (MilliporeSigma Canada Co., Ontario, Canada) was added to thoroughly dissolve the lipids, and then all solvents were evaporated overnight. The amorphous lipids formed a thin white film in the glass vial.

An aqueous solution (PGPP, PBS + Glycerol + Propylene glycol) was prepared by mixing 90 mL of phosphate-buffered saline (PBS) solution (Thermo Fisher Scientific Inc., Ontario, Canada), 5 mL of glycerol (MilliporeSigma Canada Co., Ontario, Canada), 2.5 mL of Pluronic F-68 (Thermo Fisher Scientific Inc., Ontario, Canada), and 2.5 mL of propylene glycol (MilliporeSigma Canada Co., Ontario, Canada).

Finally, the lipid mixture was dissolved in the PGPP solution and sonicated in a 50 °C water bath for 2 h. A filtration membrane (Acrodisc Syringe Filters, 3 µm pore size, VWR, Ontario, Canada) was used to remove undissolved lipids and aggregates from the solution.

2.3. Preparation of Gas Mixtures for the Generation of NBs in Microfluidics

In the experiments, gas mixtures of octafluoropropane (C_3F_8) and nitrogen (N_2) were used at various ratios. An in-house method (see **Figure 2**) was utilized to create the gas mixtures used in initial experiments that demonstrated the proof-of-concept of bubble shrinkage (see for example **Figure 3**). This enabled easy and inexpensive, albeit less accurate, adjustments to the gas mixture ratio, compared with purchasing industrially-made gas mixtures.

As shown in Figure 2, first a 500 mL measuring cylinder was filled with water, and then inverted to immerse the opening in a water-filled beaker. Then, by using control valves, different amounts of N_2 and C_3F_8 (Synquest Labs, Inc., Florida, USA) were sequentially added, at approximately equal pressures, into the measuring cylinder to create mixtures of 0.42, 4.2, and 42 wt.% C_3F_8. The volume measurements in the cylinder were used to approximate the amount of gas infused. For example, a mixture of 42 wt.% C_3F_8 was prepared by mixing 270 mL of N_2, and 30 mL of C_3F_8 in the measuring cylinder. The gas mixture in the measuring cylinder was extracted by inserting Tygon tubing that was also attached to a 50 mL syringe.

In subsequent experiments, where the focus was on detailed characterization of the NBs (Figure 5), and in both in vitro and in vivo experiments (Figures 6 and 7, respectively), an industrially made gas mixture of 99.83 wt.% N_2 and 0.17 wt.% C_3F_8 (Synquest Labs, Inc., Florida, USA) was used. This low mixing ratio was chosen such that the MB generated in the microfluidic device shrank down to sub-micron sizes.

2.4. Generation of NBs by microfluidics

2.4.1. Proof-of-Concept Experiments with the In-House Made Gas Mixture

In the initial proof-of-concept microfluidic NB generation experiments, the in-house gas mixture was supplied to the gas

© 2021 Wiley-VCH GmbH

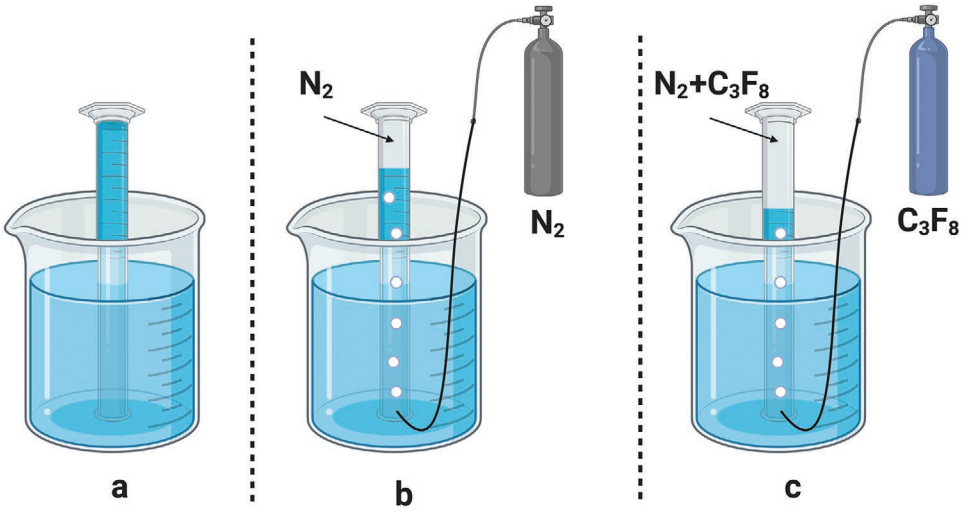

Figure 2. Schematic illustration of the in-house gas mixture created with BioRender.com. a) A 500 mL measuring cylinder is fully filled with water, before inverting to immerse the cylinder opening into a water-filled beaker. b) N_2 gas is infused into the measuring cylinder, followed by c) C_3F_8 gas, in a sequential manner, so that the gases mix at the top of the cylinder.

inlet of the device through a control valve, using Tygon tubing (Saint-Gobain S.A., Courbevoie, France) and a syringe pump (Harvard Instruments, Holliston, MA, USA). For these proof-of-concept experiments, the syringe pump flow rate was fixed at 30 mL h^{-1}. It was noted that since gas was compressible, the flow rate value on the pump did not represent the actual flow rate of the gas. Nevertheless, this injection rate, determined experimentally, was sufficiently stable to achieve a steady bubble generation regime, with approximately constant initial bubble size throughout the experiments. The continuous phase

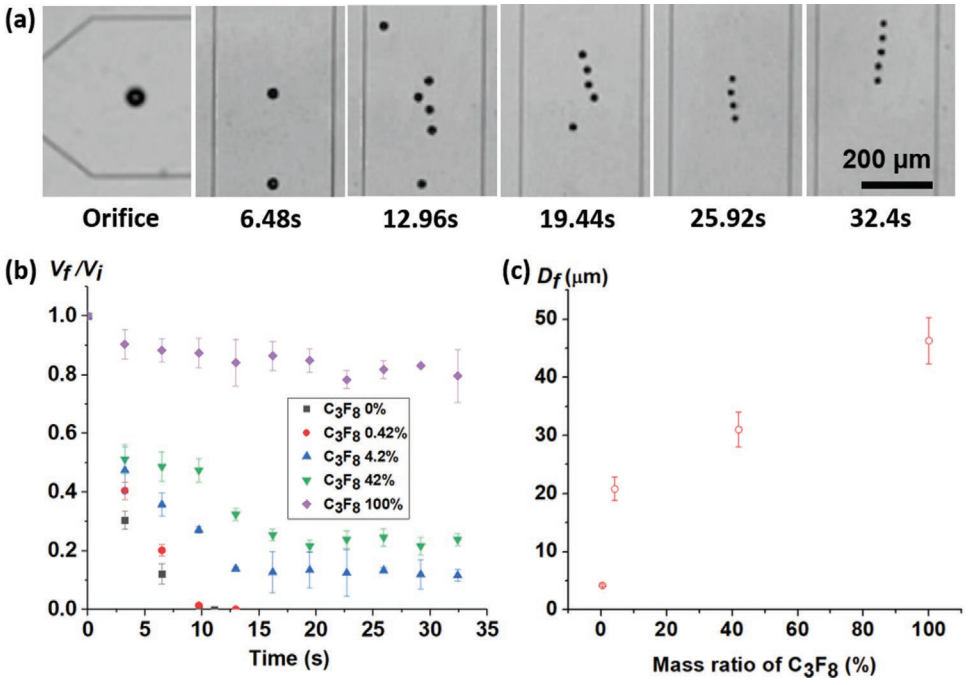

Figure 3. Proof-of-concept shrinkage of MBs of different gas-core compositions using an in-house gas mixture. a) Experimental images of the shrinkage of 4.2 wt.% C_3F_8 MBs within the serpentine channel. High speed images are taken by a brightfield microscope to track the evolution of MBs. The photos are taken in the serpentine channel after turns 10, 20, 30, 40, and 50. Each position is converted to its corresponding bubble traveling time, with the starting time at the bubble generation orifice. b) A plot of the ratio of the normalized final bubble volume V_f/V_i, versus the dissolution time of the bubbles. Here, V_f and V_i are the final and initial bubble volume, respectively. c) A plot of the final bubble diameter D_f versus the mass ratio of C_3F_8 in the gas mixture. The final diameter D_f of 0% C_3F_8 is not shown because the bubbles are completely dissolved. All of the bubbles have initial diameter of ≈50 μm, and are generated at a constant bubble generation rate of ≈100 bubbles s^{-1}. The diameter of MBs is measured using ImageJ software with the microscope photos. Each experiment is repeated three times to obtain an average and SD.

© 2021 Wiley-VCH GmbH

containing the lipid solution was supplied into the liquid inlet at a flow rate of 1 mL h^{-1} using another syringe pump.

Videos of MBs at the flow-focusing orifice, and at different positions in the serpentine channel, were captured by a high-speed camera (Miro M110, Vision Research, USA) attached to an inverted brightfield microscope (Axio Observer 7, Zeiss, Germany). The bubble sizes were measured using ImageJ software. Each measurement was repeated three times to obtain average diameters and standard deviations (SDs).

2.4.2. Experiments with the Industrially Made Gas Mixture

In later experiments, where more accurate gas mixture ratios were needed, the gas mixture was purchased from a commercial vendor, Synquest Labs Inc., Florida, USA. Here, the industrial gas mixture was supplied (0.17 wt.% C_3F_8) to the gas inlet of the device through a control valve using Tygon tubing (Saint-Gobain S.A., Courbevoie, France). The control valve was coupled to a pressure gauge which allowed to precisely control and monitor the gas pressure at the gas inlet. The continuous phase containing the lipid solution was supplied by a constant flow rate syringe pump through the liquid inlet at a flow rate of 1 mL h^{-1}.

MBs in the serpentine channel were imaged using the same approach as in the earlier proof-of-concept experiments with in-house gas mixtures. After MB shrinkage in the microchannel, the resulting NBs were collected from the outlet with a 3 mL glass vial (Figure 1d), and stored in a fridge at 4 °C before transmission electron microscopy (TEM) or resonant mass measurement (RMM) characterization.

2.5. Generation of NBs by High-Frequency Mechanical Homogenization

High-frequency mechanical homogenization was also applied to create polydisperse NBs (bulk-NBs), for comparison with the microfluidic monodisperse NBs. Bulk-NBs were generated using the same lipid solution as MF-NBs, which consisted of modifications to a previously reported protocol[48,49] as described earlier.

3 mL of the hydrated lipid solution was transferred into a 5 mL glass vial, which was then sealed with a rubber septum cap. Air from the vial was removed by creating a vacuum using a 20 mL empty syringe connected to a 25G needle. The vacuum process was repeated three times to remove most of the air from the vial. C_3F_8 gas was injected into the vial with a 10 mL syringe, prefilled with C_3F_8 gas, and a 25G needle, until the pressure in the vial was equalized. Then, another needle was immediately attached to the vial as a pressure vent and the rest of the C_3F_8 was injected to ensure the gas exchange was completed.

The glass vial containing the lipid solution and C_3F_8 gas was shaken vigorously at a frequency of 4 530 ± 100 min^{-1} for 45 s, using a mechanical shaker (VialMix, Bristol Myers Squibb, Ontario, Canada). This step generated a milky mixture of MBs and NBs.

The bubble mixture was then inverted with the rubber septum facing down and centrifuged at 500 rpm for 2 min. A 1 mL syringe and a 21G needle was used to slowly remove 1 mL of the milky solution from the bottom of the vial, where the solution consisted mostly of NBs. Finally, the NBs solution was further diluted with PBS as needed for experiments.

Importantly, polydisperse bulk-NBs by high-frequency mechanical agitation was used in the work to compare with the monodisperse MF-NBs. The same chemical formulation was utilized in both microfluidic and mechanical agitation processes. It was therefore important to recognize that the stability and ultrasound results for bulk-NBs were not generalizable to all mechanical agitation NB generation schemes, since the chemical formulation used here was not optimized for mechanical agitation. Results of mechanical homogenization using optimized formulations were different than in the literature.[47,49] For example, the polydisperse bulk-NBs used in the experiment exhibited different sizes and concentrations than the previously reported NBs made by mechanical homogenization,[49] and this difference was most likely due to the modification of the lipid solution formulation for the convenience of microfluidic bubble generation.

2.6. Characterization of NBs by TEM

For TEM imaging, a solution of 2% uranyl acetate in distilled water was used for negative staining, and the carbon-coated TEM grid was first cleaned by plasma cleaner. A 20 µL drop of NBs solution and three drops of DI water were pipetted onto a 30 cm long parafilm sheet. The liquid droplets formed the sample and dilution reservoirs, respectively. The TEM grid was gently placed on the NBs drop to contact the top of the drop and left for 2 min. The grid was then transferred to contact with the DI water drops for dilution. During each dilution step, the grid was gently placed to contact the top of the DI water drop, and kept there for 1 min. After the sample was fully diluted, 20 µL of 2% uranyl acetate was applied on the grid as a stain. Negative staining was typically done for 1 min in the dark. Excess stain was then blotted out by filter paper and the grid was air-dried before imaging.

2.7. Characterization of NBs by RMM

For quantitative NB characterization by RMM, 1 mL of NBs solution was utilized in an Eppendorf Safe-Lock microcentrifuge tube (2 mL, Eppendorf Canada, Ontario, Canada). The NB size and buoyant mass were measured using RMM (Archimedes, Malvern Instruments, UK). Specifically, an RMM nanosensor with a measurement range of 100 nm to 2 µm with a resolution limitation of 10 nm was used. The sensor was calibrated using NIST traceable 500 nm polystyrene beads (ThermoFisher 4010S, Waltham MA, USA) in water solution. The calibration was complete after 100 particles were detected.

Before sample measurements, a blank water solution was run through the RMM instrument for 5 min to ensure that the system fluidics and sensor were free of particles. It was found that a dilution with a factor of 1000 in PBS was required for the

© 2021 Wiley-VCH GmbH

bulk NBs to result in an acceptable limit of detection (LoD) of 0.01 Hz, and coincidence of <10%. Samples were loaded into the system for 90 s at a pressure of 10 psi and then analyzed at a relatively low pressure (i.e., 5 psi). Between measurements, the sensor and microfluidic tubing were rinsed for 30 s with water, followed by two "sneezes". In each sneeze step, the flow direction in the bypass and sensor channels were repeatedly reversed.

Data from the Archimedes software (version 1.2) was analyzed for positive and negative counts. Density values of 0.008 g mL^{-1} was used for positively buoyant particles (i.e., NBs) and 1.3 g mL^{-1} was used for negatively buoyant particles (i.e., lipid aggregates)[49] in the Archimedes software to convert the measured masses to particle diameters. These values were estimated experimentally using the densities of the octafluoropropane-gas-filled bubbles and the non-buoyant lipid particles, respectively.

RMM technology has intrinsic detection limitations. Therefore, in addition to the mean diameter, the final uncertainty, κ, of the size measurement was reported by combining the SD and the measurement uncertainty, $\Delta\varepsilon$.

Here, the mean of three replicates, $\varepsilon = (\varepsilon_1 + \varepsilon_2 + \varepsilon_3)/3$, where ε_1, ε_2, and ε_3 were measured NB diameter values from each replicate. The measurement uncertainty $\Delta\varepsilon$ = resolution/2 = 5 nm for an RMM resolution of 10 nm. The final uncertainty $\kappa = \sqrt{(SD)^2 + \Delta\varepsilon^2}$

2.8. Test of Long-Term Stability of NBs

The stability of MF-NBs and bulk-NBs during storage was compared. Two batches of 10 mL MF-NBs and 10 mL bulk-NBs were prepared individually per the protocols as described above, and stored at 4 °C in a fridge. At 1, 24, 48, and 72 h, 2 mL of the MF-NBs and bulk-NBs solutions were taken out from the batch and measured by RMM, respectively. Each size measurement was repeated three times. NB size measurements were reported as mean diameter plus final uncertainty, κ, to account for the resolution limitations of RMM.

2.9. In Vitro Experimental Setup

Two groups of NBs were prepared for the determination of their in vitro echogenicity. The first group consisted of microfluidically-generated NBs (MF-NBs), which were generated using the microfluidic shrinkage platform. The second group was high-frequency mechanical homogenization made NBs. These bulk-made NBs were further diluted by 1000 times so that the concentrations of MF-NBs and bulk-NBs were of the same order-of-magnitude. The bubbles were introduced into a thin ultrasound phantom (10% (w/v) gelatin) that was submerged inside a water tank. The phantom had a length of 50 mm and a diameter of 0.25 mm.

The ultrasound enhancement signals from a blank lipid solution, MF-NBs solution, and bulk-NBs solution were measured and compared. The phantom was fixed over an 18 MHz linear array transducer with 256 elements, and imaged using a pre-clinical ultrasound scanner (VisualSonics 2100, Fujifilm, Canada). System acquisition parameters were set to nonlinear contrast harmonic imaging (CHI) with 18 MHz central frequency, 35 dB dynamic range, and 40 dB gain. The power setting for the contrast mode was 4%, and power for B-mode was 1%.

2.10. In Vivo Experimental Setup

Animal experiments were conducted in compliance with St. Michael's Hospital's Animal Ethics Committee, and conformed to the Canadian Council on Animal Care guidelines.[50] In all procedures, the mice (16 weeks old, CD1 background) were anesthetized with 3% isoflurane with 1 L min^{-1} oxygen. The skin of the mouse belly was removed carefully to expose the kidney to the transducer directly, with the protection of an imaging gel.

100 µL of MF-NBs bubble solution was used in each tail vein injection, at a flow rate of 10 µL s^{-1}. CEUS images were acquired with a Vevo 2100 (Fujifilm VisualSonics) at 1 fps and 18 MHz. The power used in contrast mode and B-mode are 4% and 1%, respectively. Images were acquired from post-injection for both B-mode and non-linear mode.

3. Results and Discussions

3.1. Microfluidic Shrinkage of MBs with Gas Mixtures

We choose N_2 as the high solubility gas component, and C_3F_8 as the low solubility component. C_3F_8 is used commercially as the core gas of several UCAs.[30] MBs are first generated using a conventional PDMS microfluidic chip equipped with a flow-focusing geometry located upstream of a long serpentine channel (Figure 1a). The in-house gas mixture of N_2 and C_3F_8, introduced through the gas inlet, is pinched off at the orifice due to the viscous forces exerted by the aqueous phase. Since the aqueous phase is a lipid solution, lipid-shelled MBs are generated at the orifice (Figures 1b and 2a). The water-soluble N_2 component in the gas-core of MBs diffuses into the surrounding aqueous phase, which initiates the shrinkage of the MBs, while most of the water-insoluble C_3F_8 component remains undissolved inside the shrinking bubbles (Figure 1c). By tuning both the fraction of C_3F_8 in the gas mixture, and the flow parameters, MBs shrink down to NBs of a controllable size (Figure 1d; see Video S1, Supporting Information). We note that the collected NB solutions appear different, from mostly transparent to mostly opaque, with increasing bubble size. This appearance is most likely due to the reduction in scattering strength with a decrease in bubble size. The degree of shrinkage of MBs can be tuned by controlling the fraction of C_3F_8 in the gas mixture. With an in-house gas mixture of 4.2 wt.% C_3F_8, we observe a significant decrease in MB size along the channel (Figure 3a). We find that the time it takes for the MBs to reach a stable value of V_f/V_i increases with a higher fraction of C_3F_8 in the gas mixture (Figure 3b).

Figure 3c shows a plot of the final bubble diameter D_f versus the mass ratio of C_3F_8 in the gas mixture. Here, we determine the final bubble diameter, D_f, by measuring the bubble diameter in the serpentine channel, after the shrinkage has stopped. This

© 2021 Wiley-VCH GmbH

occurs after most of the N_2 component of the gas mixture has dissolved into the liquid, such that the gas remaining in the bubble is mostly C_3F_8.

The final diameter of NBs shows a positive correlation with the fraction of C_3F_8 in the gas mixture, which is reasonable given that C_3F_8 is supposed to a major component of the insoluble NB core. This approach is theoretically applicable to any gas mixture comprised of multiple components of different solubilities. By selecting gases of appropriate properties and controlling their mixing ratio, we can build MBs or NBs featuring different gas cores and sizes.

3.2. Shrinking MBs to NBs

We also tune the shrinkage process of MBs of fixed gas composition by controlling their initial size, which is accomplished by adjusting the gas pressure. In these experiments, we use an industrial gas mixture of 0.17 wt % C_3F_8. The evolution of MBs along the serpentine channel is shown in **Figure 4**a. In these experiments, the mass ratio of C_3F_8 in the mixture is very low, and the shrinkage of bubbles is faster than earlier experiments with higher C_3F_8 content. Figure 4b shows that bubbles with different initial sizes exhibit similar and approximately constant shrinkage rates. This observation is consistent with previous reports of dissolution of soluble gas bubbles.[51]

We obtain a maximum NB generation frequency of 10^5 s^{-1} with a gas pressure of 15 psi and a liquid flow rate of 3 mL hr^{-1}, which leads to a final bubble concentration of $\approx 10^8$ mL^{-1}. Further scale-up of the production throughput is possible by optimizing the microfluidic design, employing higher flow rates and gas pressures, parallelizing flow-focusing orifices,[52] and concentrating MBs with microcavity trapping structures,[53] followed by subsequent shrinkage to NBs. Importantly, this method generates NBs without significant changes to typical microfluidic bubble preparation methods, and without needing to improve the manufacturing resolution of microfluidic devices.

NBs are collected for further characterization. We use RMM technology to obtain size distributions. We confirm that MF-NBs have smaller sizes and better monodispersity compared to bulk-NBs made by high-frequency homogenization, even after some post-processing by centrifugation (see **Figure 5**a and Experimental Section).

With the assumption that most of the N_2 gas dissolves in the liquid, and most of the C_3F_8 gas remains in the bubble, we expect that $D_f \propto D_i$, and this is supported experimentally in Figure 5b. This relationship indicates that with a fixed gas mixture composition, monodispersed NBs of specific sizes can be obtained by tuning the initial size of the MBs, which can be easily achieved with a typical flow-focusing microfluidic device.

We choose RMM as the primary measurement technique because it is the only method[49] capable of distinguishing between NBs of positive buoyancy[54,55] and lipid particles or surfactant aggregates of negative buoyancy. In contrast, characterizations based on dynamic light scattering cannot easily distinguish between these two groups. The RMM results in Figure 5a are also supported by TEM imaging (Figure 5c), which shows clear differences between MF-NBs, bulk-NBs, and the lipid solution background. Specifically, the MF-NBs exhibit better monodispersity than the bulk-NBs.

We note a sharp cutoff in the RMM measured size distribution observed for buoyant NBs, and attribute this result to the LoD of the RMM sensor (see for example Figure 5a). The cutoff observed in the graph occurs at the smallest size in the distribution, which corresponds approximately to the LoD of the sensor. The LoD is automatically determined by RMM system at the start of each measurement and accounts for the baseline noise. We do not use any thresholding or post-processing to reject smaller-sized particles.

3.3. NB Stability

The stability of NBs in solution is investigated by tracking their size changes over time (**Table 1**). We note that the measurements here are near the LoD of RMM, which likely truncates the size distribution. However, the impact of systematic errors should be the same for both MF-NB and bulk-NB samples. The

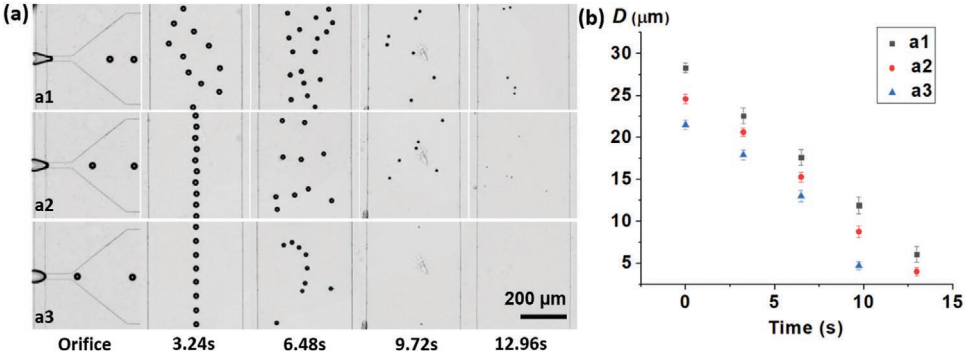

Figure 4. Shrinkage of MBs of different initial sizes, with the same industrially made gas mixture. a) Experimental images of different initial size MBs along the serpentine channel. The leftmost images are taken at the orifice, and the labels 3.24s, 6.48s, 9.72s, 12.96s correspond to time in the channel after serpentine channel turns 5, 10, 15, and 20. Experiments a1, a2, and a3 have initial bubble diameters, D_i = 28.3, 24.6, and 21.5 μm, respectively. b) A plot of instantaneous bubble diameter D versus evolution time. The flow rate of the lipid solution is constant at 1 mL h^{-1}, and the bubble generation rate of $\approx 10^3$ s^{-1} is maintained approximately constant. Diameter of MBs is measured using ImageJ software according to the microscope photos. Each experiment is repeated three times to obtain an average and SD.

© 2021 Wiley-VCH GmbH

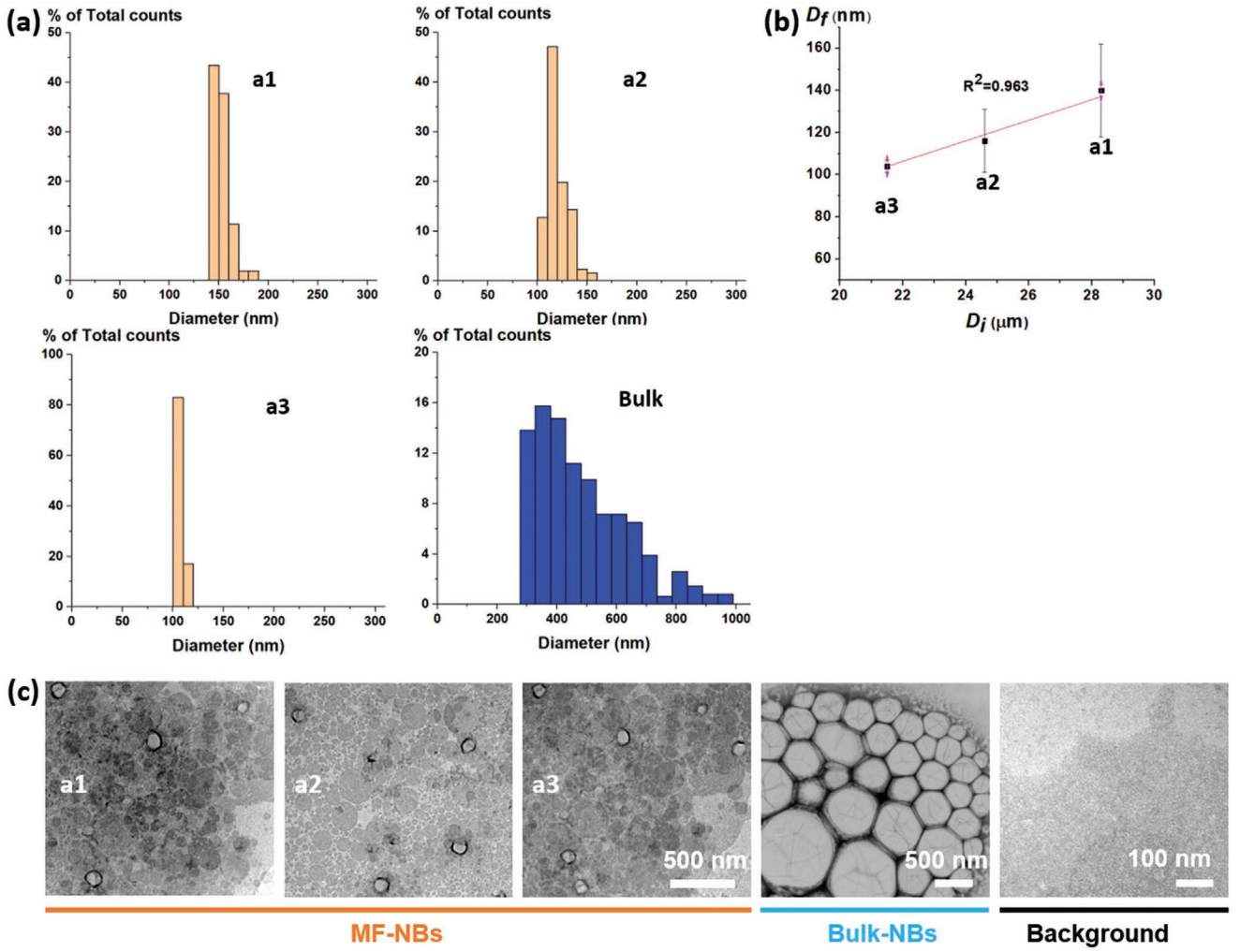

Figure 5. Characterization of NBs shrinking from MBs of different initial sizes, with the same industrial gas mixture. a) Size measurements of final NBs of experiments a1, a2, and a3 by RMM. Bulk-NBs are prepared using high-frequency homogenization as the control group. b) A plot of final bubble diameter D_f versus initial diameter D_i. c) Morphology characterization of MF-NBs and bulk-NBs by TEM. The MF-NBs, bulk-NBs, and blank background as control are shown as labeled. The NBs in a1, a2, and a3 have initial bubble diameters, D_i = 28.3, 24.6, and 21.5 μm, respectively, as demonstrated in Figure 4. Diameter of NBs is measured using RMM. Each experiment is repeated three times to obtain an average and SD.

Table 1. Evolution of NB sizes over time. The sizes and concentrations of 2 mL of MF-NBs and bulk-NBs at 1, 24, 48, and 72 h are measured by RMM. Each size measurement is repeated three times. NB size measurements are reported as mean diameter plus final uncertainty, κ, to account for the resolution limitations of RMM. The concentrations of both MF-NBs and bulk-NBs remain within the same order-of-magnitude over 72 h. Each experiment is repeated three times to obtain an average and SD.

MF-NBs	1 h	24 h	48 h	72 h
Mean Diameter [nm] ±κ	156 ± 7	148 ± 6	146 ± 5	152 ± 13
Polydispersity ± SD	0.11 ± 0.04	0.08 ± 0.02	0.07 ± 0.03	0.15 ± 0.04
Concentration		≈10^7 mL^{-1}		
Bulk-NBs	1 h	24 h	48 h	72 h
Mean Diameter [nm] ±κ	223 ± 11	202 ± 9	227 ± 13	188 ± 6
Polydispersity ± SD	0.32 ± 0.14	0.26 ± 0.07	0.39 ± 0.02	0.3 ± 0.05
Concentration		≈10^8 mL^{-1}		

© 2021 Wiley-VCH GmbH

results show that MF-NBs and bulk-NBs exhibit similar stability over 72 h without significant change of bubble concentrations. However, MF-NBs maintain lower polydispersity than bulk-NBs over the same duration. This is likely due to NBs of approximately equal sizes in a monodisperse population being less susceptible to Ostwald ripening than those in a polydisperse population.[56]

3.4. In Vitro Ultrasound Imaging

We evaluate the echogenicity of the NBs in in vitro imaging experiments (**Figure 6**a). Here, monodisperse MF-NBs are generated using the industrial gas mixture (0.17 wt.% C_3F_8, see Video S2, Supporting Information). We make polydisperse bulk-NBs using the modified bulk mechanical homogenization approach[49] followed by centrifugal size isolation[57] and dilute the sample to a similar NB concentration as MF-NBs. We use two common ultrasound imaging modes, brightness (B)-mode, and non-linear CEUS mode, to compare the echogenicity of MF-NBs and bulk-NBs. Specifically, B-mode records and processes the echo of a tissue/organ to form a gray-scale image of the internal structure,[58] while the non-linear CEUS mode is based on an amplitude modulation that forms images by subtracting signals obtained under low and high pressures. In non-linear CEUS, echoes from linear scatterers are predominantly canceled, while echoes from non-linear scatterers (such as NBs) appear.[59]

Figure 6b shows the results of in vitro ultrasound imaging of blood vessel phantoms. We observe that monodisperse MF-NBs exhibit an enhanced signal homogeneity compared to polydisperse bulk-NBs, with comparable brightness. We attribute this improvement to the better monodispersity of MF-NBs, which can be hard to achieve by traditional bulk preparation methods even with extensive filtration and differential centrifugation. The monodisperse MF-NBs scatter ultrasound waves more uniformly than the polydisperse bulk-NBs (Figure 6b). This difference is likely due to the wider range of bubble sizes in bulk-NBs (Table 1). We also observe that MF-NBs exhibit a comparable non-linear contrast enhancement to bulk-NBs (Figure 6c), at 1 min post-injection. This result suggests that the MF-NBs are usable as contrast agents with good signal homogeneity and enhancement.

3.5. In Vivo Ultrasound Imaging

In in vivo imaging experiments of mouse kidneys (**Figure 7**a) the brightness of the non-linear contrast mode images is significantly enhanced (Figure 7b). Like in artificial blood vessel phantoms, MF-NBs show good signal uniformity in the live mouse kidney, which indicates that the MF-NBs remain stable and monodisperse in the physiological environment.

Qualitatively, we observe that the signal intensity increases significantly starting at ≈6–7 s post-injection, which shows MF-NBs arriving at the kidney region (see Figure 7c). An enhancement intensity peak is achieved between 9 and 10 s post-injection (see Video S3, Supporting Information), which corresponds to the time the injection is completed, and the intensity enhancement from MF-NBs stabilizes after this initial peak.

The MF-NBs in this experiment exhibit shorter imaging lifetime than more conventional polydisperse bulk NBs, made by mechanical homogenization using an optimized lipid mixture, and at much higher bubble concentration.[49] However, we note that the MF-NBs exhibit an obvious signal enhancement

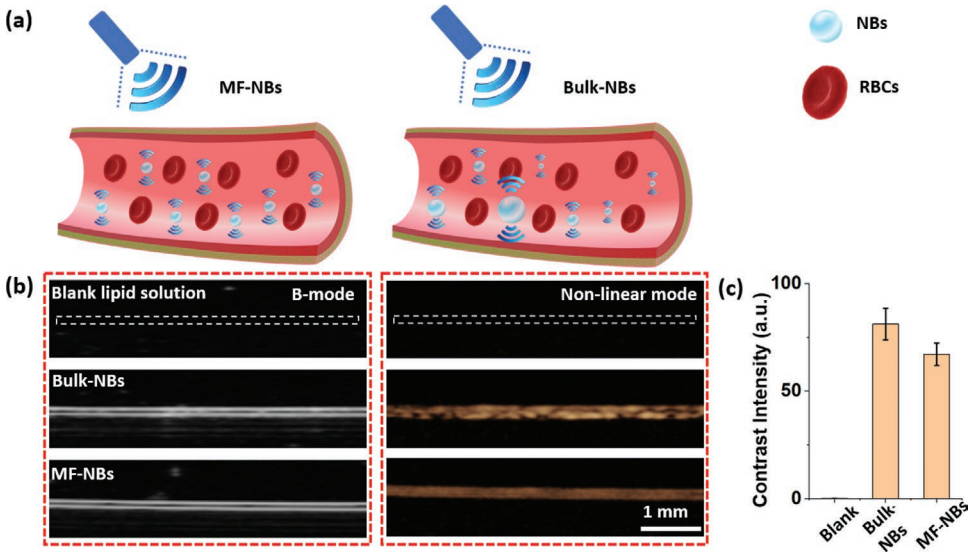

Figure 6. In vitro CEUS imaging with NBs. a) Illustration comparing the ultrasound echoes of MF-NBs (left) and bulk-NBs (right) in blood vessels created with BioRender.com. b) Representative in vitro ultrasound images of NBs under different contrast modes: B-mode (left), and non-linear mode (right), in a blood-vessel-like phantom filled with saline. The white dashed rectangle represents regions of interest (ROI) for quantitative analyses. c) Plot of non-linear CEUS signal intensity enhancement (post-injection intensity minus pre-injection intensity) at 1 min post-injection from blank lipid solution, bulk-NBs, and MF-NBs. The NBs are characterized by RMM: MF-NBs have diameter 328 ± 49 nm ($n = 3$), concentration ≈10^7 mL^{-1}, and polydispersity (PDI) 0.148; Bulk-NBs have diameter 418 ± 121 nm ($n = 3$), concentration ≈10^7 mL^{-1}, and PDI 0.288. Scale bar represents 1 mm.

© 2021 Wiley-VCH GmbH

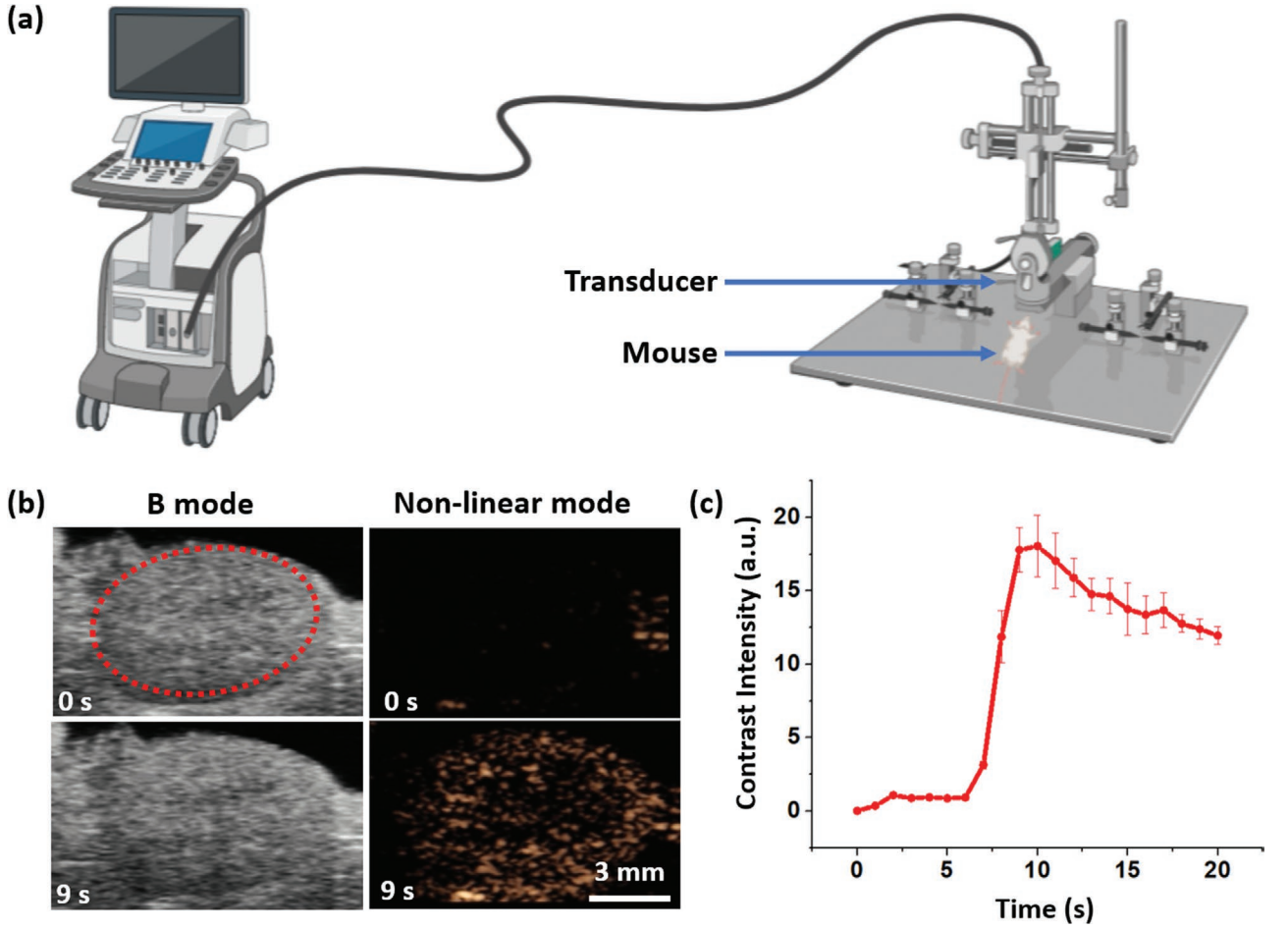

Figure 7. Proof-of-concept in vivo CEUS imaging with MF-NBs. a) Schematic diagram of the experimental setup created with BioRender.com. b) Representative images from in vivo ultrasound imaging experiments of a mouse kidney, with NBs, under B-mode and non-linear mode. The red dashed ellipses represent the ROI for quantitative analyses. The images are taken at 0 s and 9 s after the injection of the MF-NBs solution. c) Plot of real-time ultrasound signal intensity enhancement (post-injection intensity minus pre-injection intensity) versus time from MF-NBs in non-linear CEUS mode. The MF-NBs in the in vitro and in vivo imaging experiments are from the same batch, with diameter 328 ± 49 nm (n = 3), concentration ≈10^7 mL^{-1}, and polydispersity (PDI) 0.148. The ultrasound transducer is applied directly to the surface of mouse kidneys for imaging. Scale bar represents 3 mm.

despite having a lower bubble concentration. One explanation for the stronger echo activity of the MF-NBs may be the non-linear scattering enhanced by shell buckling of NBs that may increase echogenicity.[60] The non-linear contrast imaging mode uses multiple ultrasound pulses for which the amplitude of the pulse is modulated to detect the non-linear response of the bubbles. Another possibility is that, for monodisperse MF-NBs, constructive interactions of the collective nonlinear behavior of interacting bubble clusters may be more likely to happen compared to bulk NBs.[61]

A current limitation of the microfluidic approach is the resulting NB concentration, which is ≈10^8 mL^{-1}. However, the system geometry and flow conditions can still be optimized to produce higher concentrations and throughput, for example, via parallel flow focusing.[62] In clinical situations, tissues such as tumors may have various depths or vascularity that can lead to a choice of NB concentration based on the imaging goals. For example, one may wish to achieve specific target echogenicities at different imaging depths. The results here demonstrate advantages of microfluidically made monodisperse NBs, which may find applications in diagnostic ultrasound imaging, therapeutic ultrasound, and in situ micro- or nano-surgery.

4. Conclusion

We describe, for the first time, size-tunable and monodisperse NBs generated using a simple microfluidic approach. Controlling the fraction of insoluble and soluble gas components of the bubble gas core and tuning the initial size of bubbles generated at a flow-focusing microfluidic geometry enables the production of NBs of different target sizes. Compared to NB production protocols that generate polydisperse NBs, our microfluidic method improves controllability and uniformity of NBs and retains a tunable concentration (up to 10^8 mL^{-1}) of bubbles. MF-NBs show better signal uniformity than polydisperse NBs in in vitro ultrasound imaging experiments, and result in good signal homogeneity as well as contrast enhancement in in vivo ultrasound imaging experiments.

© 2021 Wiley-VCH GmbH

This work may enable new opportunities for ultrasound imaging and therapy. Unlike intravascular contrast agent MBs, which are currently used clinically, NBs in principle can exit the vasculature and extravasate into certain tissues due to the EPR effect[63] around intermittently permeable tumor regions. Since tissues do not produce sub-harmonic or super-harmonic signals as NBs do, NBs that extravasate into tissues can be considered UCAs suitable for molecular imaging.

Supporting Information

Supporting Information is available from the Wiley Online Library or from the author.

Acknowledgements

S.S.H.T. and M.C.K. acknowledge financial support from the Canadian Natural Sciences and Engineering Research Council (NSERC) Strategic Projects grant program (No. STGP 506318) and infrastructure support from the Canada Foundation for Innovation (CFI), Ontario Research Fund (ORF), and Ryerson University. D.Y. is grateful for funding from the Canadian Institutes of Health Research (CIHR) New Investigator Award. The authors are grateful for early discussions with Dr. V. Gnyawali, and ongoing discussions with Dr. Raffi Karshafian, and MD Precision Inc.

Conflict of Interest

The authors declare no conflict of interest.

Author Contributions

J.X. led all experiments and wrote the manuscript. A.S. contributed to the fabrication of microfluidic chips and proof-of-concept experiments. Y.X. and X.H. performed the in vitro and in vivo experiments. L.K. helped with the bubble shrinkage experiments and resonant mass measurements. A.D. performed the TEM characterizations. D.Y. contributed to the design of the in vivo experiments and provided animal samples. A.C.L. and A.A.E assisted in developing lipid formation protocols and bulk NB generation experiments. S.S.H.T and M.C.K. conceptualized, organized, and supervised this project. All authors participated in the discussion of ideas and results and editing of the manuscript.

Data Availability Statement

The data that support the findings of this study are available from the corresponding author upon reasonable request.

Keywords

bio-imaging, microbubbles, microfluidics, nanobubbles

Received: January 18, 2021
Revised: February 26, 2021
Published online: April 2, 2021

[1] H. Tsuge, *Micro-and Nanobubbles: Fundamentals and Applications*, CRC press, Boca Raton, FL **2014**.
[2] D. Lohse, X. Zhang, *Rev. Mod. Phys.* **2015**, *87*, 981.
[3] C. Huang, J. Jiang, M. Lu, L. Sun, E. I. Meletis, Y. Hao, *Nano Lett.* **2009**, *9*, 4297.
[4] S. Li, Y. Du, T. He, Y. Shen, C. Bai, F. Ning, X. Hu, W. Wang, S. Xi, X. Zhou, *J. Am. Chem. Soc.* **2017**, *139*, 14277.
[5] P.-G. de Gennes, *Langmuir* **2002**, *18*, 3413.
[6] J. Zhu, H. An, M. Alheshibri, L. Liu, P. M. Terpstra, G. Liu, V. S. Craig, *Langmuir* **2016**, *32*, 11203.
[7] K. K. T. Phan, T. Truong, Y. Wang, B. Bhandari, *Food Eng. Rev.* **2020**, *1*, 12.
[8] C. Kim, R. Qin, J. S. Xu, L. V. Wang, R. X. Xu, *J. Biomed. Opt.* **2010**, *15*, 010510.
[9] T. Yin, P. Wang, R. Zheng, B. Zheng, D. Cheng, X. Zhang, X. Shuai, *Int. J. Nanomed.* **2012**, *7*, 895.
[10] K. Hettiarachchi, E. Talu, M. L. Longo, P. A. Dayton, A. P. Lee, *Lab Chip* **2007**, *7*, 463.
[11] R. Perera, C. Hernandez, M. Cooley, O. Jung, S. Jeganathan, E. Abenojar, G. Fishbein, A. J. Sojahrood, C. C. Emerson, P. L. Stewart, *Nanoscale* **2019**, *11*, 15647.
[12] C.-H. Wang, Y.-F. Huang, C.-K. Yeh, *Langmuir* **2011**, *27*, 6971.
[13] S. Mo, C.-C. Coussios, L. Seymour, R. Carlisle, *Expert Opin. Drug Delivery* **2012**, *9*, 1525.
[14] Y. Gao, C. Hernandez, H.-X. Yuan, J. Lilly, P. Kota, H. Zhou, H. Wu, A. A. Exner, *Nanomedicine* **2017**, *13*, 2159.
[15] V. Paefgen, D. Doleschel, F. Kiessling, *Front. Pharmacol.* **2015**, *6*, 197.
[16] H. Maeda, J. Wu, T. Sawa, Y. Matsumura, K. Hori, *J. Controlled Release* **2000**, *65*, 271.
[17] E. Y. Lukianova-Hleb, Y.-S. Kim, I. Belatsarkouski, A. M. Gillenwater, B. E. O'Neill, D. O. Lapotko, *Nat. Nanotechnol.* **2016**, *11*, 525.
[18] A. Helbert, E. Gaud, T. Segers, C. Botteron, P. Frinking, V. Jeannot, *Ultrasound Med. Biol.* **2020**, *46*, 3339.
[19] T. Segers, P. Kruizinga, M. P. Kok, G. Lajoinie, N. de Jong, M. Versluis, *Ultrasound Med. Biol.* **2018**, *44*, 1482.
[20] N. Nirmalkar, A. Pacek, M. Barigou, *Langmuir* **2019**, *35*, 2188.
[21] Z. Xing, J. Wang, H. Ke, B. Zhao, X. Yue, Z. Dai, J. Liu, *Nanotechnology* **2010**, *21*, 145607.
[22] M. Xie, J. Zhang, Y. Chen, C. Deng, L. Zhang, Z. Sun, J. Wang, Y. Yang, Q. Lv, W. Han, *Front. Pharmacol.* **2019**, *10*, 610.
[23] J. L. Parker, P. M. Claesson, P. Attard, *J. Phys. Chem.* **1994**, *98*, 8468.
[24] N. Ishida, T. Inoue, M. Miyahara, K. Higashitani, *Langmuir* **2000**, *16*, 6377.
[25] S.-T. Lou, Z.-Q. Ouyang, Yi Zhang, *J. Vac. Sci. Technol., B: Microelectron. Nanometer Struct.–Process., Meas., Phenom.* **2000**, *18*, 2573.
[26] X. H. Zhang, X. D. Zhang, S. T. Lou, Z. X. Zhang, J. L. Sun, J. Hu, *Langmuir* **2004**, *20*, 3813.
[27] Q. Chen, L. Luo, H. S. White, *Langmuir* **2015**, *31*, 4573.
[28] S. R. German, Q. Chen, M. A. Edwards, H. S. White, *J. Electrochem. Soc.* **2016**, *163*, H3160.
[29] E. Kang, H. S. Min, J. Lee, M. H. Han, H. J. Ahn, I. C. Yoon, K. Choi, K. Kim, K. Park, I. C. Kwon, *Angew. Chem., Int. Ed. Engl.* **2010**, *49*, 524.
[30] A. Upadhyay, S. V. Dalvi, *Ultrasound Med. Biol.* **2019**, *45*, 301.
[31] E. Castro-Hernández, W. van Hoeve, D. Lohse, J. M. Gordillo, *Lab Chip* **2011**, *11*, 2023.
[32] D. Das, K. Sivasubramanian, C. Yang, M. Pramanik, *Sci. Rep.* **2018**, *8*, 1.
[33] A. H. Dhanaliwala, A. J. Dixon, D. Lin, J. L. Chen, A. L. Klibanov, J. A. Hossack, *Biomed. Microdevices* **2015**, *17*, 1.
[34] P. Garstecki, A. Gańán-Calvo, G. Whitesides, *Bull. Pol. Acad. Sci.: Tech. Sci.* **2005**, *53*, 361.
[35] N. Xiang, H. Yi, K. Chen, S. Wang, Z. Ni, *J. Micromech. Microeng.* **2013**, *23*, 025016.
[36] L.-F. Tsai, W. C. Dahlquist, S. Kim, G. P. Nordin, *J. Micro/Nanolithogr., MEMS, MOEMS* **2011**, *10*, 043009.

© 2021 Wiley-VCH GmbH

[37] A. Salari, J. Xu, M. C. Kolios, S. S. Tsai, *Phys. Rev. Fluids* **2020**, *5*, 013602.
[38] E. Castro-Hernandez, W. van Hoeve, D. Lohse, J. M. Gordillo, *Lab Chip* **2011**, *11*, 2023.
[39] S. Ganta, H. Devalapally, A. Shahiwala, M. Amiji, *J. Controlled Release* **2008**, *126*, 187.
[40] A. H. Dhanaliwala, J. L. Chen, S. Wang, J. A. Hossack, *Microfluid. Nanofluid.* **2013**, *14*, 457.
[41] S. A. Peyman, J. R. McLaughlan, R. H. Abou-Saleh, G. Marston, B. R. Johnson, S. Freear, P. L. Coletta, A. F. Markham, S. D. Evans, *Lab Chip* **2016**, *16*, 679.
[42] V. Gnyawali, B.-U. Moon, J. Kieda, R. Karshafian, M. C. Kolios, S. S. Tsai, *Soft Matter* **2017**, *13*, 4011.
[43] J. Xu, S. Zhang, A. Machado, S. Lecommandoux, O. Sandre, F. Gu, A. Colin, *Sci. Rep.* **2017**, *7*, 4794.
[44] J. I. Park, Z. Nie, A. Kumachev, E. Kumacheva, *Soft Matter* **2010**, *6*, 630.
[45] T. Segers, E. Gaud, G. Casqueiro, A. Lassus, M. Versluis, P. Frinking, *Appl. Phys. Lett.* **2020**, *116*, 173701.
[46] Y. Y. C. Sang, E. Lorenceau, S. Wahl, M. Stoffel, D. E. Angelescu, R. Höhler, *RSC Adv.* **2013**, *3*, 2330.
[47] T. M. Krupka, L. Solorio, R. E. Wilson, H. Wu, N. Azar, A. A. Exner, *Mol. Pharmaceutics* **2010**, *7*, 49.
[48] W. B. Cai, H. L. Yang, J. Zhang, J. K. Yin, Y. L. Yang, L. J. Yuan, L. Zhang, Y. Y. Duan, *Sci. Rep.* **2015**, *5*, 13725.
[49] C. Hernandez, E. C. Abenojar, J. Hadley, R. Coyne, R. Perera, R. Gopalakrishnan, J. P. Basilion, M. C. Kolios, A. A. Exner, *Nanoscale* **2019**, *11*, 851.
[50] E. D. Olfert, B. M. Cross, A. A. McWilliam, *Guide to the care and use of experimental animals*, Vol. *1*, Canadian Council on Animal Care Ottawa, Ottawa, Canada **1993**.
[51] R. M. Detsch, *J. Geophys. Res.: Oceans* **1990**, *95*, 9765.
[52] H. Lin, J. Chen, C. Chen, *Med. Biol. Eng. Comput.* **2016**, *54*, 1317.
[53] Y. Gao, M. Wu, Y. Lin, J. Xu, *Lab Chip* **2020**, *20*, 4512.
[54] T. P. Burg, M. Godin, S. M. Knudsen, W. Shen, G. Carlson, J. S. Foster, K. Babcock, S. R. Manalis, *Nature* **2007**, *446*, 1066.
[55] M. Godin, F. F. Delgado, S. Son, W. H. Grover, A. K. Bryan, A. Tzur, P. Jorgensen, K. Payer, A. D. Grossman, M. W. Kirschner, *Nat. Methods* **2010**, *7*, 387.
[56] E. Talu, K. Hettiarachchi, R. L. Powell, A. P. Lee, P. A. Dayton, M. L. Longo, *Langmuir* **2008**, *24*, 1745.
[57] J. A. Feshitan, C. C. Chen, J. J. Kwan, M. A. Borden, *J. Colloid Interface Sci.* **2009**, *329*, 316.
[58] K. K. Shung, *J. Med. Biol. Eng.* **2011**, *31*, 6.
[59] A. Needles, M. Arditi, N. Rognin, J. Mehi, T. Coulthard, C. Bilan-Tracey, E. Gaud, P. Frinking, D. Hirson, F. Foster, *Ultrasound Med. Biol.* **2010**, *36*, 2097.
[60] A. JafariSojahrood, L. Nieves, C. Hernandez, A. Exner, M. C. Kolios, in *2017 IEEE Int. Ultrasonics Symp. (IUS)*, IEEE **2017**, pp. 1–4.
[61] H. Haghi, A. Sojahrood, M. C. Kolios, *Ultrason. Sonochem.* **2019**, *58*, 104708.
[62] X. Kang, C. Luo, Q. Wei, C. Xiong, Q. Chen, Y. Chen, Q. Ouyang, *Microfluid. Nanofluid.* **2013**, *15*, 337.
[63] P. Nittayacharn, H.-X. Yuan, C. Hernandez, P. Bielecki, H. Zhou, A. A. Exner, *J. Pharm. Sci.* **2019**, *108*, 3091.

© 2021 Wiley-VCH GmbH